2005

Integral field spectroscopy of 23 spiral bulges

Dan Batcheldor

David Axon

David Merritt

Recommended Citation
Astrophysical Journal Supplement Series 160N1 (Sep 2005) 76

The Astrophysical Journal Supplement Series
Preprint typeset using LaTeX style emulateapj v. 11/26/04

INTEGRAL FIELD SPECTROSCOPY OF 23 SPIRAL BULGES

D. Batcheldor,[1,2] D. Axon,[2,1] D. Merritt,[2] M. A. Hughes,[1] A. Marconi,[3] J. Binney,[4] A. Capetti,[5] M. Merrifield,[6] C. Scarlata,[7] and W. Sparks[8]

Received 2005 March 17; accepted 2005 April 27

ABSTRACT

We have obtained Integral Field Spectroscopy for 23 spiral bulges using INTEGRAL on the William Herschel Telescope and SPIRAL on the Anglo-Australian Telescope. This is the first 2D survey directed solely at the bulges of spiral galaxies. Eleven galaxies of the sample do not have previous measurements of the stellar velocity dispersion (σ_*). These data are designed to complement our Space Telescope Imaging Spectrograph program for estimating black hole masses in the range $10^6 - 10^8 M_\odot$ using gas kinematics from nucleated disks. These observations will serve to derive the stellar dynamical bulge properties using the traditional Mgb and CaII triplets. We use both Cross Correlation and Maximum Penalized Likelihood to determine projected σ_* in these systems and present radial velocity fields, major axis rotation curves, curves of growth and σ_* fields. Using the Cross Correlation to extract the low order 2D stellar dynamics we generally see coherent radial rotation and irregular velocity dispersion fields suggesting that σ_* is a non-trivial parameter to estimate.

Subject headings: integral field spectroscopy - galaxies: spiral - galaxies: velocity distributions

1. INTRODUCTION

The increasing number of super-massive black hole (SMBH) candidates discovered in the mid 1990s led to the investigation of SMBH demographics. It was found that various properties of the host bulge correlated with the SMBH mass, e.g. bulge luminosity and mass (Kormendy & Richstone 1995; Magorrian et al. 1998), stellar velocity dispersion - the $M_\bullet - \sigma_*$ relation - (Ferrarese & Merritt 2000; Gebhardt et al. 2000) and concentration index (Graham et al. 2003). Scatter in these relations are comparable if enough care is taken in deriving the bulge properties (Marconi & Hunt 2003). Such correlations have fundamental implications for both SMBH and host galaxy formation and evolution. These "secondary" methods also present a valuable practical tool to estimate SMBH mass. The "primary" methods, used to originally define the relations, determine SMBH mass by considering the direct gravitational effects of SMBHs. However, each primary method has a drawback: proper motion studies can only be carried out in the Milky Way; H_20 masers need to be orientated correctly; gas kinematics may be influenced by non-gravitational effects and stellar dynamics must be derived from relatively low surface brightnesses. The advantages of knowing the exact form of the SMBH - host relations then become obvious if trying to sample a large number of SMBH masses across a wide dichotomy of host types and redshifts.

There still exists a fundamental bias toward large ($\sim 10^9 M_\odot$) SMBH mass measurements in the relations however. This stems from the relative ease of mass measurements in giant ellipticals: it is easier to spot a bigger black hole. The low mass end of the relations ($10^6 M_\odot < M_\bullet < 10^8 M_\odot$), which essentially represents late type spirals, has yet to be fully populated. This is unsurprising when considering the difficulties and complexities involved with observing and modelling such systems. This swing toward high mass SMBHs has led some to discuss whether these relations are indeed linear (Laor 2001).

If we are to effectively extrapolate these secondary relations to make conclusions about formation and evolutionary scenarios, and indeed use them as SMBH mass estimators, we need to quell any doubts as to their nature. To this end we have completed a Space Telescope Imaging Spectrograph (STIS) survey of 54 local spirals (Hughes et al. 2003; Scarlata et al. 2004) using the *Hubble Space Telescope* (*HST*). This data has been used to make primary SMBH mass estimates by modelling the gravitational potential as represented by the central gas kinematics and surface brightness profiles (Marconi et al. 2003; Atkinson et al. 2005). However, to populate the low mass end of the secondary estimators we need to establish the bulge properties. Consequently we have initiated integral field spectroscopic observations of the original STIS sample. Integral Field Spectroscopy (IFS) is a reliable and highly flexible tool capable of quickly gathering a large amount of dynamical information. It allows the observation of the full 2D Line of Sight Velocity Distributions (LOSVDs).

As there are few published 2D kinematical maps of spiral bulges we present here an atlas of our data so far including radial velocity fields, major axis rotation curves, stellar velocity dispersion (σ_*) fields and aperture integrated velocity dispersions (curves of growth). In § 2 we outline the observations and basic data reduction, while

[1] Centre for Astrophysics Research, STRI, University of Hertfordshire, Hatfield, AL10 9AB, UK; danb@star.herts.ac.uk
[2] Department of Physics, Rochester Institute of Technology, 84 Lomb Memorial Drive, Rochester, NY, 14623, USA.
[3] INAF-Osservatorio Astrofisico di Arcetri, Largo E. Fermi 5, 50125 Firenze, Italy.
[4] Oxford University, Theoretical Physics, Keble Road, Oxford, OX1 3NP, UK.
[5] INAF-Osservatorio Astronomico di Torino, I-10025 Pino Torinese, Italy.
[6] School of Physics and Astronomy, University of Nottingham, NG7 2RD, UK.
[7] Eidgenoessische Technische Hochshule Zürich, Hönggerberg HPF G4.3, CH-8092 Zürich, Switzerland.
[8] Space Telescope Science Institute, 3700 San Martin Drive, Baltimore, MD, 21218, USA.

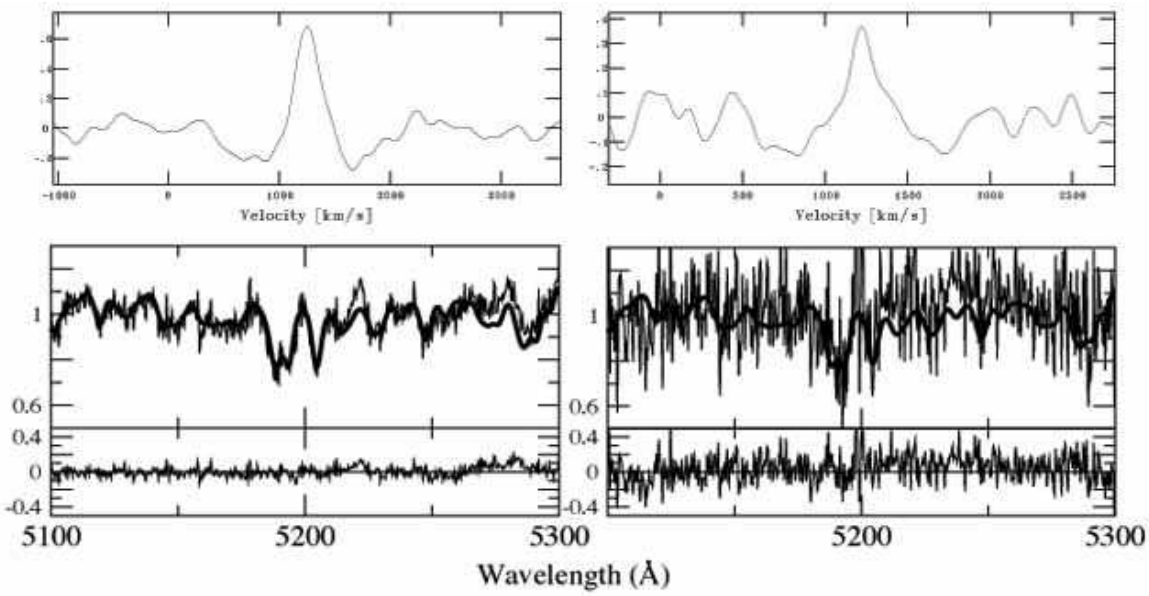

FIG. 1.— Demonstrating the Xcor fits to the data. [top row] The left panel shows the cross correlation function derived from a S/N=23 spectrum in NGC 4041, while the right panel details the function in a S/N=8 case. [bottom row] The bold lines show the fits using the derived parameters to the observed spectra. The lower sections present the residuals of the fits.

§ 3 details how we extracted the 2D LOSVDs. The data is presented in § 4 and briefly summarized and discussed in § 5.

2. OBSERVATIONS AND DATA REDUCTION

Our observations form the first IFS survey specifically applied to a sample of spiral bulges. They positively complement the SAURON IFS project which is directed at 72 targets including a number of spirals (de Zeeuw et al. 2002; Emsellem et al. 2004). From the nature of the $M_\bullet - \sigma_*$ relation, and the general character of spiral galaxies, we required instruments capable of resolving σ_* well below 100 km s^{-1}. For our northern hemisphere targets this lead us to use the fibre fed Integral Field Unit (IFU) INTEGRAL, on the 4.2m WHT, with the 5$^{\rm th}$ order Echelle grating ($\Re \approx 6000$). Whilst the CaII triplet is the preferred tracer of stellar dynamics (Dressler 1984) this grating could only be centered on the Mgb triplet (~ 5200Å). Observing conditions ensured all nights were non-photometric and forced the use of the SB3 fibre bundle. This bundle consists of a main $33\farcs6 \times 29\farcs4$ array with 115 circular apertures[9] packed according to Kepler's Conjecture. The $2\farcs7$ diameter of these apertures ensured that the PSF due to seeing (which was typically $1\farcs5$) was under-sampled. The main array is surrounded by a concentric circle ($\oslash 90''$) of 20 apertures designed to sample the sky. For our southern hemisphere targets we used the fibre fed IFU SPIRAL, on the 3.9m AAT, with the R1200 grating ($\Re \approx 7600$) centered on the CaII triplet at ~ 8660Å. Ordinarily SPIRAL consists of 512 apertures but effective sky reduction can be achieved by masking half of the array and using SPIRAL in "nod and shuffle" (NS) mode. NS masking of the MITLL2A detector meant that 1 row and 1 column of the array fell off the chip. This reduced the number of usable apertures ($\oslash 0\farcs7$) to 225 over a $11'' \times 9\farcs8$ area.

During our observing runs priority was given to targets for which we have successful STIS spectra (Hughes et al. 2003). To date we have completed IFS observations on 23 of the original 54 spiral bulges. Calibration frames including flat-fields, tungsten lamp flats, dark frames, bias frames and Cu-Ne/Cu-Ar arc frames, along with at least 3 late type (G, K, M) spectroscopic standards, were observed throughout each night. At least 3 target exposures were made in order to facilitate the easy removal of cosmic rays. We made several offset sky observations, especially when the overheads associated with NS observations lead us to abandon its use in some cases. The SPIRAL data was reduced using the adapted automatic 2df software developed by Jeremy Bailey of the Anglo-Australian Observatory. INTEGRAL data reduction was carried out with standard IRAF[10] routines, and made use of the *integral* package developed by Robert Greimel of the Isaac Newton Group. Detector positions of the individual aperture spectra were traced by fitting a polynomial across the dispersion axis of a high signal lamp flat. This enabled scattered light to be identified and removed from the science frames. The trace of the spectra was then used as a master template in extracting the subsequent spectra. Lamp flats were again used to make throughput corrections before carrying out wavelength calibrations. Sky subtraction was performed using NS or by subtracting a collapsed off-set sky frame or summed sky apertures. All objects had the continuum fitted to each individual spectra. This level was then used together with the aperture spacial positions to create 2D intensity maps (essentially very low spacial resolution images of the targets).

3. EXTRACTING LOSVDS

Since the early 1970s there have been a multitude of techniques employed to extract dynamical information from digitized spectra (Simkin 1974; Sargent et al.

[9] Throughout "apertures" means the individual fibres, lenslets or spaxels referred to in other IFS studies.

[10] IRAF is distributed by the National Optical Astronomy Observatories, which are operated by the Association of Universities for Research in Astronomy, Inc., under co-operative agreement with the National Science foundation.

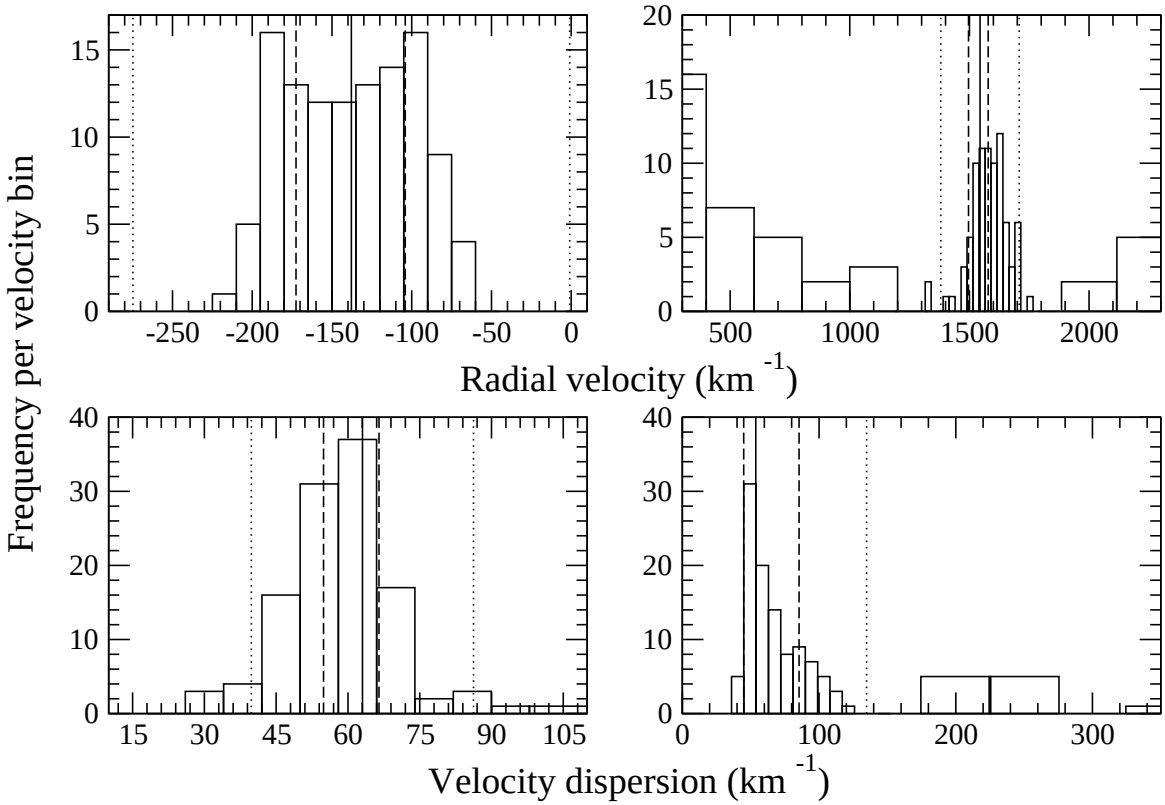

FIG. 2.— Identifying discordant data. In all cases the solid line marks the median value and the dashed lines show the upper and lower quartiles. The dotted lines mark the $2i \pm m$ boundaries, where m is the median and i is the inter-quartile range. Data falling outside of the dotted lines were marked as discordant. [left column] NGC 4212. The top panel presents the radial velocities and the bottom panel shows the velocity dispersions in this low discordant example. [right column] Same as the left column but for NGC 3021; a high discordant example.

1977; Franx, Illingworth & Heckman 1989; Bender 1990; Rix & White 1992; van der Marel & Franx 1993; Kuijken & Merrifield 1993; Merritt 1997; Cappellari & Emsellem 2004). In general each method makes the fundamental assumption that LOSVDs can be recovered by convolving a broadening function to a shifted template stellar spectra of the same mean spectral type. We have attempted to use each of these methods on our sample, but only a select few are suited to the nature of our data (essentially $\sim$ 3500 S/N$\approx$ 10 spectra). Typical Fourier and pixel fitting techniques fail at the levels of S/N present here and require a large amount of time to complete due to the nature of filters and number of possible solutions. We have seen that the technique of Cross Correlation, hereafter Xcor (Tonry & Davies 1979, TD79), performed well in extracting accurate 1st and 2nd order LOSVD moments from our spectra and is particularly suited to large datasets.

We performed Xcor on each spectrum for each observed template by following TD79 as implemented in the *iraf.rvsao* package. As these reduction steps are considered standard and well established we refer readers wishing to see the detailed treatment of spectra through the cross correlation procedure to Kurtz & Mink (1998). In brief, the position of the Xcor peak determines the radial velocity shift, whilst the width of the peak is related to the projected stellar velocity dispersion (σ_*). Each spectrum has any residual emission features suppressed and is continuum subtracted, apodized, zero-padded and binned linearly in log space before being passed through the Xcor. Quadratic weights are applied to deviations in the continuum subtracted spectra to ensure that stronger lines are more heavily weighted. To limit the size of secondary peaks in the Xcor function a cosine bell filter is applied.

Errors in the position and width of the Xcor are defined by the "r" statistic which is calculated by *rvsao* and is used as a quality measure of the Xcor. If we assume that a perfect Xcor is proportional to the broadening function convolved with the Auto Correlation Function (ACF, i.e., the Xcor of a spectrum with itself) then we expect to see symmetry about the radial velocity. This is because both the broadening function and the ACF are themselves symmetrical. The constant of proportionality between the perfect correlation and the convolved broadening function will be defined by the height of the central peak. The height of the peak, normalized by the anti-symmetric components in the Xcor, defines r and is used as the aforementioned quality measure of values derived from the Xcor itself.

However, these error estimates are insignificant when compared to those introduced by the possibility of template mismatch, low signal spectra and large velocity dispersions. The advantages of observing a template library now becomes apparent. For each aperture, after correcting the Xcor radial velocities for barycentric and stellar radial velocities, we used the r weighted average value between each template for the velocity and width measured in that aperture. The standard deviation around these weighted values was then used as a separate estimate in the error of each measurement. More weight

TABLE 1
Main Results for the Sample

Galaxy	% DC	Peak S/N	$\sigma_{\rm ce}$ (km s^{-1})	$\sigma_{\rm cc}$ (km s^{-1})	$\sigma_{\rm me}$ (km s^{-1})	$\sigma_{\rm mc}$ (km s^{-1})	h_3	h_4
NGC 0289	30.4	19.69	95 ± 10	114 ± 14	93^{+41}_{-29}	111^{+47}_{-24}	$0.02^{+0.01}_{-0.05}$	$0.26^{+0.03}_{-0.02}$
NGC 0613	29.6	20.70	113 ± 1	99 ± 2	201^{+9}_{-10}	149^{+19}_{-22}	$-0.14^{+0.02}_{-0.05}$	$0.11^{+0.08}_{-0.07}$
NGC 1255	16.5	10.94	57 ± 1	69 ± 5	34^{+32}_{-9}	47^{+27}_{-3}	$-0.14^{+0.09}_{-0.12}$	$0.09^{+0.13}_{-0.03}$
NGC 1300	11.3	21.40	87 ± 5	90 ± 6	86^{+32}_{-13}	82^{+55}_{-19}	$0.12^{+0.01}_{-0.20}$	$0.16^{+0.06}_{-0.11}$
NGC 1832	13.0	15.98	88 ± 3	102 ± 13	104^{+11}_{-13}	129^{+16}_{-18}	$-0.09^{+0.09}_{-0.08}$	$0.03^{+0.04}_{-0.04}$
NGC 2748	17.4	20.98	83 ± 8	79 ± 7	107^{+7}_{-10}	78^{+3}_{-7}	$0.00^{+0.06}_{-0.07}$	$-0.02^{+0.05}_{-0.05}$
NGC 2903	33.0	25.84	89 ± 4	95 ± 6	138^{+5}_{-6}	171^{-0}_{-6}	$-0.12^{+0.08}_{-0.10}$	$0.15^{+0.09}_{-0.14}$
NGC 2964	19.1	29.33	103 ± 12	111 ± 14	138^{+28}_{-18}	135^{+40}_{-26}	$0.07^{+0.11}_{-0.09}$	$0.21^{+0.03}_{-0.05}$
NGC 3021	40.0	14.54	82 ± 3	125 ± 7	81^{+74}_{-1}	62^{+45}_{-15}	$-0.08^{+0.07}_{-0.06}$	$0.12^{+0.15}_{-0.12}$
NGC 3162	24.4	14.18	70 ± 2	85 ± 1	80^{+11}_{-10}	82^{+12}_{-7}	$-0.12^{+0.04}_{-0.01}$	$0.07^{+0.02}_{-0.04}$
NGC 3310	26.1	27.74	84 ± 1	101 ± 1	127^{+25}_{-19}	115^{+15}_{-17}	$0.01^{+0.01}_{-0.08}$	$0.15^{+0.04}_{-0.10}$
NGC 3949	38.3	18.95	82 ± 2	80 ± 3	113^{+17}_{-12}	75^{+7}_{-7}	$0.00^{+0.03}_{-0.05}$	$0.21^{+0.03}_{-0.06}$
NGC 3953	12.2	19.95	116 ± 3	146 ± 1	122^{+4}_{-8}	127^{+13}_{-12}	$0.02^{+0.01}_{-0.02}$	$-0.01^{+0.04}_{-0.01}$
NGC 4041	11.3	22.93	88 ± 7	92 ± 8	97^{+7}_{-3}	96^{+5}_{-6}	$0.04^{+0.06}_{-0.04}$	$0.00^{+0.04}_{-0.04}$
NGC 4051	40.0	45.05	72 ± 10	91 ± 10	92^{+19}_{-15}	126^{+30}_{-20}	$1.7^{+0.5}_{-0.9}$	$2.1^{+0.3}_{-0.6}$
NGC 4088	27.0	15.46	77 ± 2	87 ± 4	88^{+8}_{-9}	117^{+25}_{-18}	$0.00^{+0.04}_{-0.04}$	$0.11^{+0.04}_{-0.03}$
NGC 4212	4.4	21.05	75 ± 2	82 ± 5	62^{+3}_{-4}	67^{+6}_{-4}	$-0.02^{+0.14}_{-0.10}$	$0.07^{+0.04}_{-0.11}$
NGC 4258	20.9	39.38	148 ± 4	120 ± 6	126^{+9}_{-4}	140^{+12}_{-6}	$-0.01^{+0.01}_{-0.02}$	$-0.02^{+0.01}_{-0.01}$
NGC 4303	23.5	29.71	84 ± 3	108 ± 2	102^{+2}_{-6}	133^{+10}_{-22}	$-0.06^{+0.04}_{-0.03}$	$0.01^{+0.02}_{-0.03}$
NGC 4321	16.5	21.33	83 ± 3	101 ± 2	95^{+7}_{-5}	109^{+6}_{-16}	$-0.07^{+0.04}_{-0.03}$	$0.11^{+0.03}_{-0.02}$
NGC 4536	37.4	14.62	85 ± 1	168 ± 13	182^{+16}_{-20}	190^{+7}_{-24}	$0.01^{+0.08}_{-0.04}$	$0.02^{+0.07}_{-0.07}$
NGC 5005	10.4	53.71	154 ± 10	203 ± 11	190^{+7}_{-6}	213^{+7}_{-10}	$0.06^{+0.04}_{-0.03}$	$0.05^{+0.03}_{-0.02}$
NGC 5055	12.2	47.12	117 ± 6	118 ± 5	124^{+5}_{-4}	122^{+7}_{-4}	$0.04^{+0.02}_{-0.02}$	$0.04^{+0.03}_{-0.01}$

Note. — "% DC" refers to the percentage of discordant data. "$\sigma_{\rm ce}$" indicates extended Xcor values, "$\sigma_{\rm cc}$" central Xcor, "$\sigma_{\rm me}$" extended MPL and "$\sigma_{\rm mc}$" central MPL. "h_3" and "h_4" are for the higher LOSVD moments in the central apertures.

was placed on higher r values as defined in the following equation:

$$\bar{\phi_F} = \frac{\sum_{i=1}^{3} \phi_i r_i^2}{\sum_{i=1}^{3} r_i^2} \quad (1)$$

where ϕ_F is the final velocity or width and $\phi_{1..3}$ and $r_{1..3}$ represent the values derived using template 1,2 or 3. Any of the weighted values that fell outside the equivalent of a 2.7σ clip (defined by the interquartile range of the data from the entire array) were flagged as "discordant", the percentage of discordant events per galaxy then being used as a quality measure of the IFS data.

As with the intensity maps, the full 2D kinematics were recovered by mapping the derived velocities to the relative spacial positions of each aperture on the IFUs.

We have carried out extensive testing of the Xcor procedure by creating a composite spectra from the observed templates, generating simulated radial velocity and velocity dispersion fields, introducing a surface brightness profile and adding Poisson noise. As the width of the Xcor peak does not give a direct measure of σ_* we tested three independent σ_* recovery methods: HWHM correction ($\sigma\sqrt{2\ln 2}$); ACF correction ($\sigma^2 = \mu^2 - 2\tau^2$, where μ is the width of the peak and τ is given by the ACF) and a calibration function correction. The calibration function, which was determined by fitting a polynomial to the known and measured values of σ_*, proved to be far superior in terms of χ^2. As some of our sample are known to contain starbursts and AGN we also tested the effects that such objects may have on the Xcor. To the composite template spectrum we added increasing proportions of early type spectra and a Seyfert 1 spectrum. In both cases we found that 90% contamination was needed in order to significantly affect the r statistic (i.e., take it below 3). Similar results were also found when introducing large velocity shifts to spectra (~ 3000 km s^{-1}).

Examples of the Xcor are presented in Figures 1 and 2. Figure 1 shows the cross correlation functions from two apertures in NGC 4041 and overlays of the derived fits onto observed spectra. In both the high signal (S/N=23) and low signal (S/N=8) cases well defined cross correlation functions can be seen giving confident results. These Figures also demonstrate the nature of the r statistic (the amount of anti-symmetry in the cross correlation function). Figure 2 demonstrates how discordant data was identified and flagged. The two cases presented show both low and high discordance observations. The derived radial velocity and velocity dispersion data from low discordance and high discordance cases (NGC 4212 and NGC 3021 respectively) were placed into discrete bins in velocity space. The distribution of data is shown by plotting the number of measurements to fall within a specific bin.

In spectra down to S/N≈ 5 we are confident that the Xcor procedure will return accurate values for the 1$^{\rm st}$ and 2$^{\rm nd}$ order LOSVD moments. However, in many cases the central apertures of the IFU arrays contain S/N > 15.

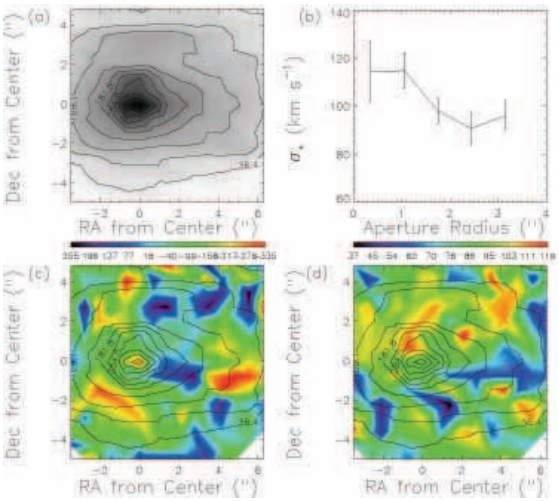

FIG. 3.— Xcor results for NGC 0289. (a) 2D intensity map. (b) Curve of growth. (c) Radial Velocity Field (km s^{-1}). (d) σ_* Field (km s^{-1}). Full color plots can be found in the electronic version.

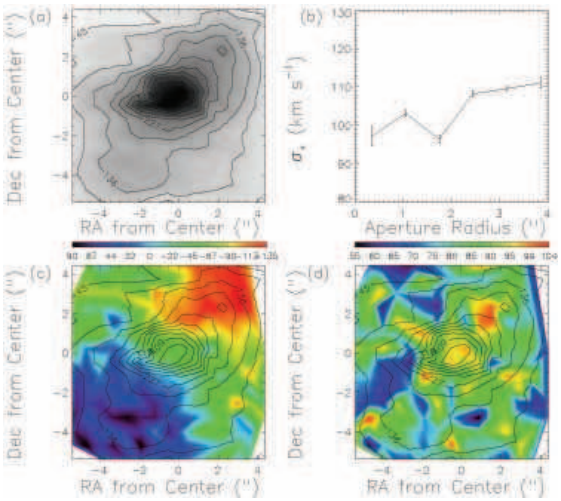

FIG. 4.— Same as Figure 3 but for NGC 0613.

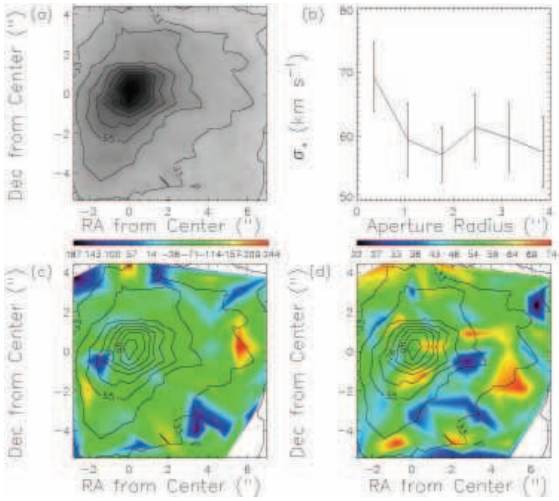

FIG. 5.— Same as Figure 3 but for NGC 1255.

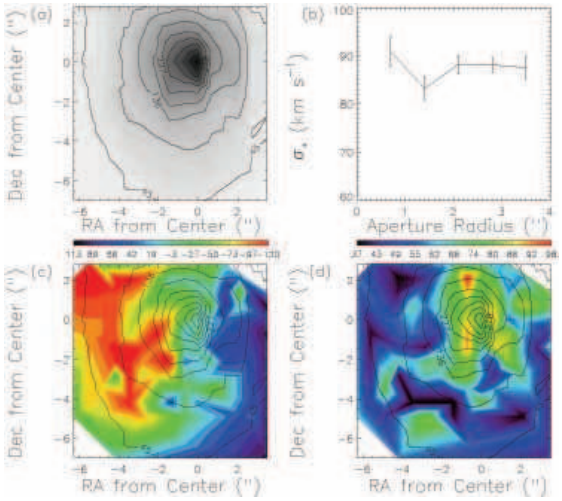

FIG. 6.— Same as Figure 3 but for NGC 1300.

Here we can attempt to recover higher order moments (h_3 and h_4) which harbor further dynamical information on the observed system, i.e., signatures of SMBHs. Performing LOSVD extraction via an independent technique also provides a valuable verification of previous results. The Maximum Penalized Likelihood, hereafter MPL (Merritt 1997), is a non-parametric method in that it places no constraints on the shape of the LOSVD and allows the recovery of higher order moments ($h_0 ... h_6$). It is ideally suited to low S/N as the penalty function introduces significantly less bias than Fourier methods when smoothing noise characteristics. We carried out similar tests as for the Xcor and again found that 90% starburst/AGN contamination and shifts of > 3000 km s^{-1} were needed to significantly affect the extracted moments. In order to determine the most appropriate value for the smoothing parameter (α) we re-performed the MPL for increasing values of α until cusps in the higher moments were seen. A bootstrap, using 100 realizations, was used in order to determine the 68% confidence levels in the derived Hermite polynomials.

4. RESULTS, VELOCITY FIELDS AND COMMENTS FOR INDIVIDUAL GALAXIES

The main results for our sample are presented in Table 1. We have provided measures of σ_* taken from the central aperture of each array (determined by the peak value of σ_* closest to the photometric center of the target - "central" apertures) and also σ_* measured from spectra collapsed across the entire arrays ("extended" apertures). We also present, for each galaxy, intensity maps derived from the continuum level of each spectra, the "curve of growth" derived by determining σ_* through progressively larger collapsed apertures, the radial velocity field and the velocity dispersion field. In all cases North is up and East is to the left. In the cases where there is evidence of a net rotation the radial velocities along the major axes have also been presented. We continue by making comments on each galaxy.

4.1. *NGC 0289*

Figure 3. The data are noisy and almost 1/3 is excluded as discordant. As a consequence nothing can be said about the 2D dynamics. These are the first measures of σ_* in NGC 289.

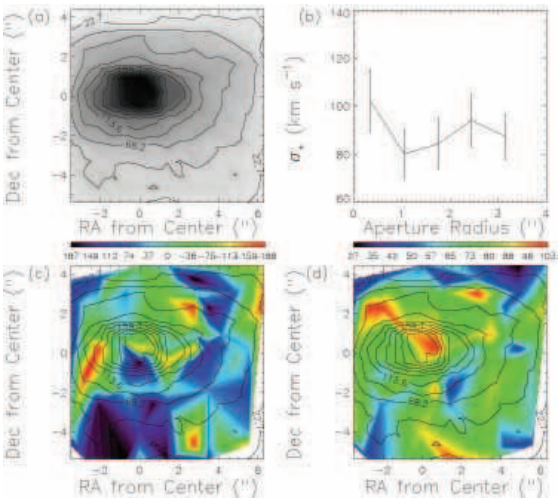

FIG. 7.— Same as Figure 3 but for NGC 1832.

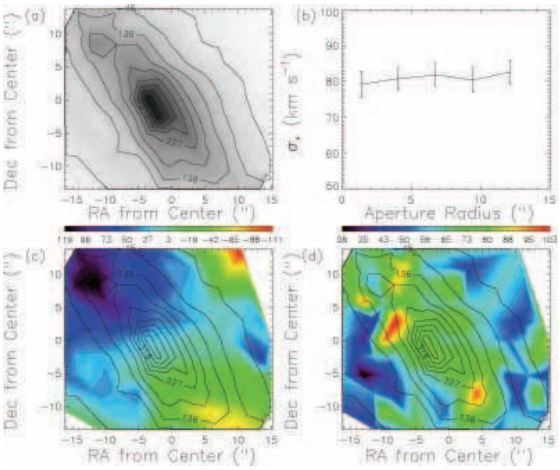

FIG. 8.— Same as Figure 3 but for NGC 2748.

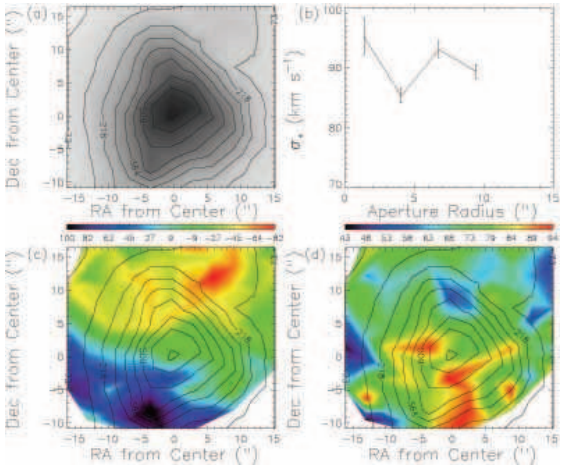

FIG. 9.— Same as Figure 3 but for NGC 2903.

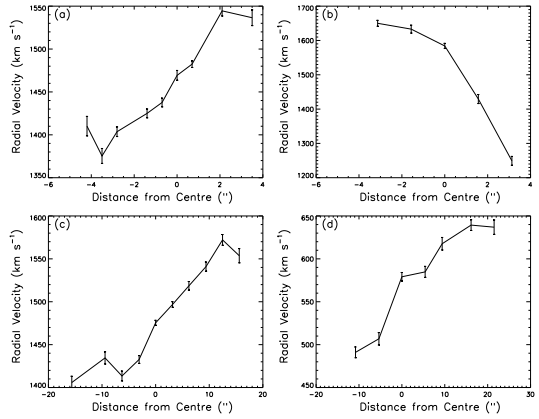

FIG. 10.— Radial velocity curves taken along the major axes of each galaxy. Numbers in square brackets refer to the position angle in degrees (east from north) along which the curves have been extracted. (a) NGC 613 [135]. (b) NGC 1300 [90]. (c) NGC 2748 [30]. (d) NGC 2903 [150].

4.2. *NGC 0613*

Figures 4 and 10(a). Clearly defined rotation despite a high level of discordance. The σ_* field is patchy but a significant difference between extended and central values of σ_* is noted. There are also significant values of h_3 and h_4 corresponding to a central asymmetric non-Gaussian LOSVD.

4.3. *NGC 1255*

Figure 5. S/N is low in all spectra but the level of discordance is also low. No clear rotation can be seen and the σ_* field is patchy. These are the first measures of σ_* in NGC 1255.

4.4. *NGC 1300*

Figures 6 and 10(b). A low level of discordance and good S/N has produced a velocity field showing rotation and a clear centrally peaked σ_* field. Color maps suggest possible obscuration from spiral structures (Hughes et al. 2003).

4.5. *NGC 1832*

Figure 7. The levels of S/N are low and the radial velocity and σ_* fields are noisy. There is a significant difference between central and extended values of σ_*. These are the first measures of σ_* in NGC 1832.

4.6. *NGC 2748*

Figures 8 and 10(c). Typical S/N and discordance. Clear rotation and patchy σ_*. NGC 2748 has an inclination of $\sim 70°$ which could account for LOSVD obscuration especially in the presence of dust lanes (Hughes et al. 2003). These are the first measures of σ_* in NGC 2748 and are constant with aperture radius.

4.7. *NGC 2903*

Figures 9 and 10(d). High level of discordance but S/N is good. Clear rotation and an irregular σ_* field. MPL did not converge in the central aperture. A known star-burst with a circumnuclear ring (Alonso-Herrero, Ryder & Knapen 2001).

4.8. *NGC 2964*

Figures 11 and 17(a). Good S/N with clear rotation and a centrally peaked σ_* field. Slight central peak in the curve of growth. Significant amounts of dust (Hughes et al. 2003).

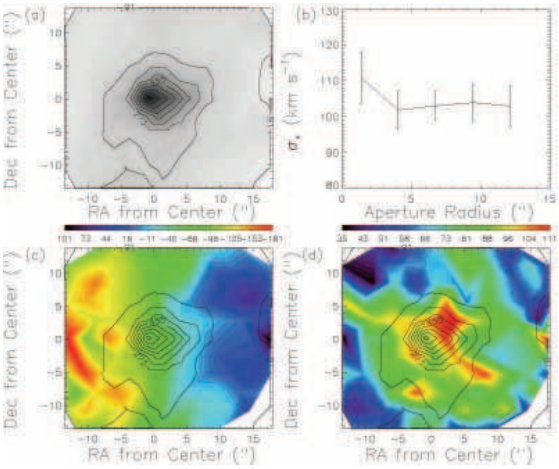

FIG. 11.— Same as Figure 3 but for NGC 2964.

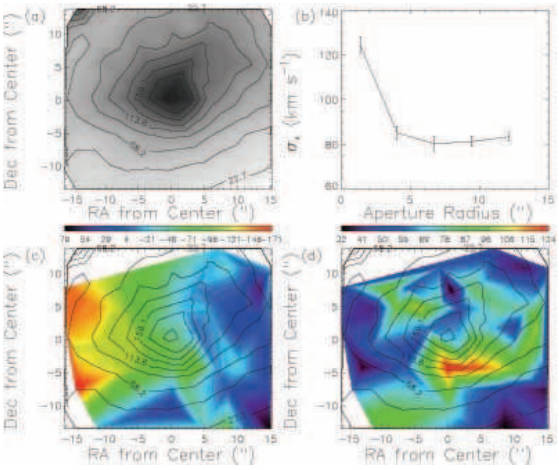

FIG. 12.— Same as Figure 3 but for NGC 3021.

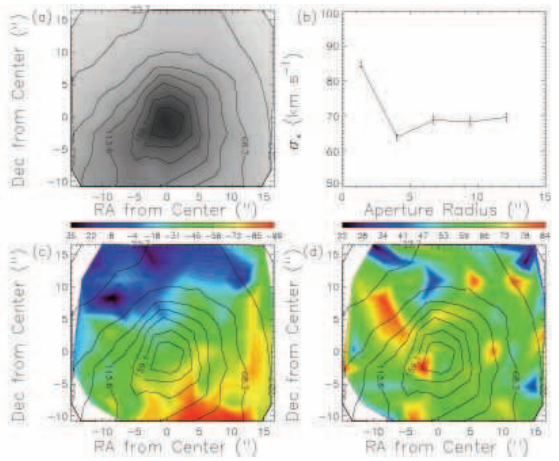

FIG. 13.— Same as Figure 3 but for NGC 3162.

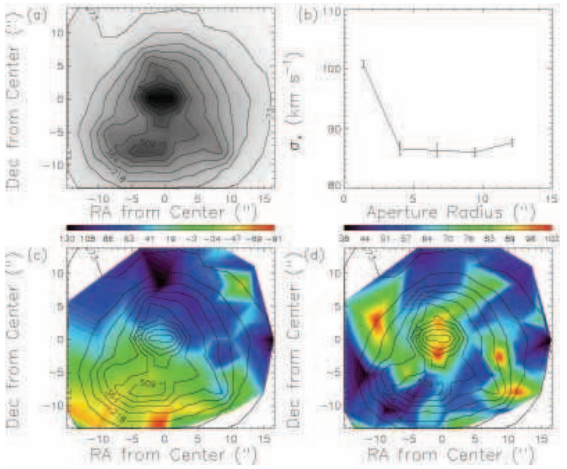

FIG. 14.— Same as Figure 3 but for NGC 3310.

4.9. *NGC 3021*

Figures 12 and 17(b). Significant discordance and low S/N. Clear rotation and a peaked σ_* field. Significant difference between extended and central apertures.

4.10. *NGC 3162*

Figures 13 and 17(c). Low S/N and typical discordance. Clear rotation and irregular σ_* field. Significant difference between extended and central apertures. There are central asymmetries in the LOSVD. These are the first measures of σ_* in NGC 3162.

4.11. *NGC 3310*

Figures 14 and 17(d). Good S/N and typical discordance. Clear rotation, patchy σ_* field and a clear difference between central and extended σ_*. Possible high velocity components in central LOSVD. Significant amounts of dust (Hughes et al. 2003).

4.12. *NGC 3949*

Figures 15 and 20(a). High discordance and fair S/N. Clear rotation and irregular σ_* field. Constant curve of growth. Significant high velocity components in the central LOSVD. Thin dust lane (Hughes et al. 2003). These are the first measures of σ_* in NGC 3949.

4.13. *NGC 3953*

Figures 16 and 20(b). Low discordance and good S/N. Centrally peaked σ_* field and clear rotation. Large central curve of growth peak. There are no previous measures of σ_* for NGC 3953.

4.14. *NGC 4041*

Figures 18 and 20(c). Good S/N and low discordance. Fairly constant curve of growth, regular rotation and a centrally peaked σ_* field. Nuclear star cluster (Marconi et al. 2003). There are no previous measures of σ_* for NGC 4041.

4.15. *NGC 4051*

Figures 19 and 20(d). Significant discordance and low S/N. The large peak signal is due to the AGN. Regular rotation, patchy σ_* field and a steep curve of growth. There are large values for both h_3 and h_4, the signature of a large asymmetry and super-Gaussian wings in the LOSVD.

4.16. *NGC 4088*

Figures 21 and 26(a). Low S/N and high discordance. Clear rotation and a patchy σ_* field. A significant central peak in the curve of growth. The inclination of

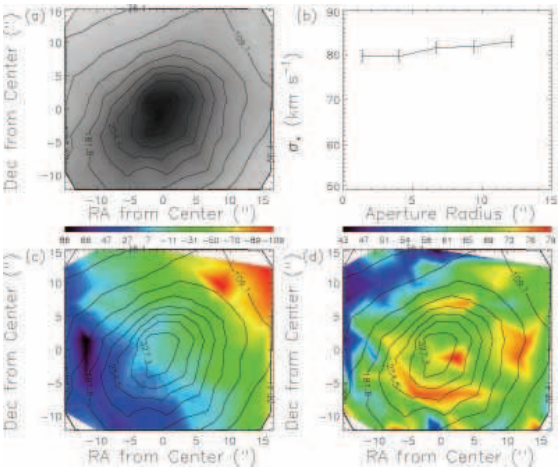

FIG. 15.— Same as Figure 3 but for NGC 3949.

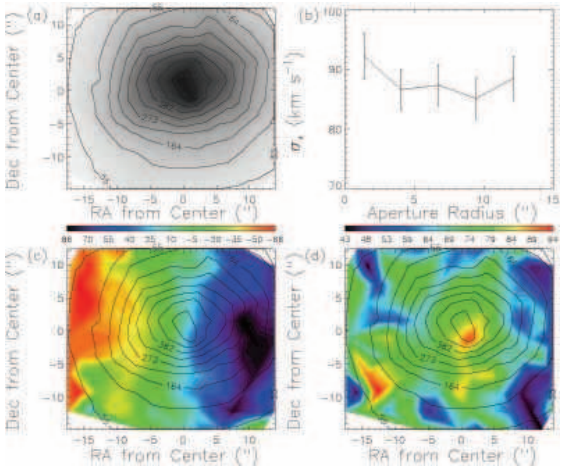

FIG. 18.— Same as Figure 3 but for NGC 4041.

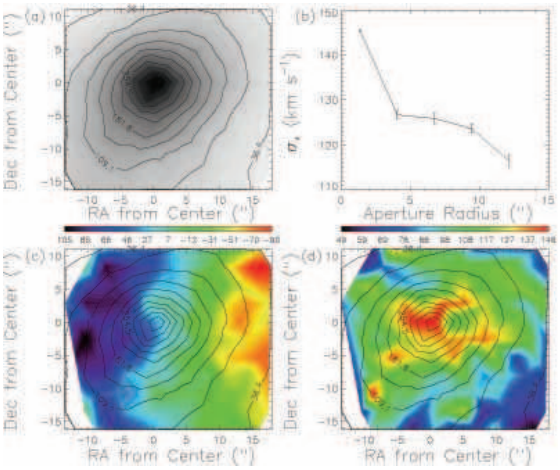

FIG. 16.— Same as Figure 3 but for NGC 3953.

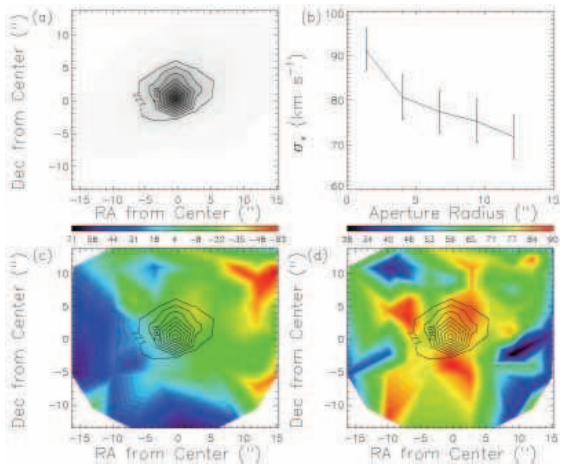

FIG. 19.— Same as Figure 3 but for NGC 4051.

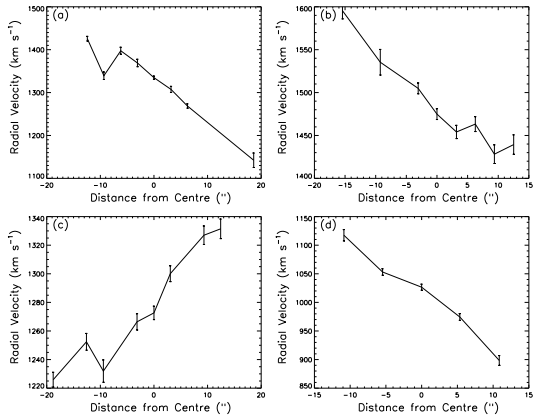

FIG. 17.— Same and Figure 10 but for (a) NGC 2964 [90]. (b) NGC 3021 [90]. (c) NGC 3162 [30]. (d) NGC 3310 [0].

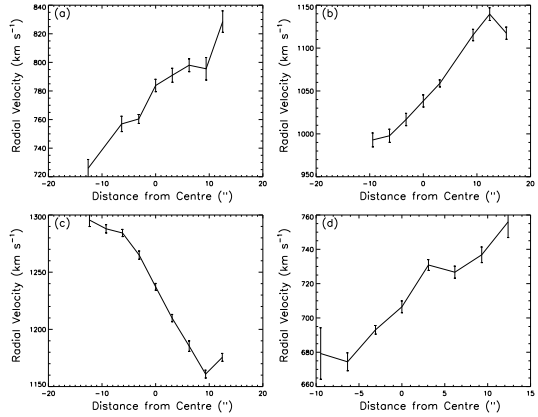

FIG. 20.— Same as Figure 10 but for (a) NGC 3949 [120]. (b) NGC 3953 [90]. (c) NGC 4041 [90]. (d) NGC 4051 [120].

NGC 4088 ($\sim 71°$) suggests there may be some obscuration from the disk. These are the first measures of σ_* in NGC 4088.

4.17. *NGC 4212*

Figures 22 and 26(b). Remarkably low discordance and good signal. Centrally peaked σ_* field, clear regular rotation and a significant peak in the curve of growth. There are no previous measures of σ_* for NGC 4212.

4.18. *NGC 4258*

Figures 23 and 26(c). Typical discordance and excellent S/N. Clearly defined rotation and an irregular σ_* field. NGC 4258 is inclined at $\sim 72°$ and exhibits a dust

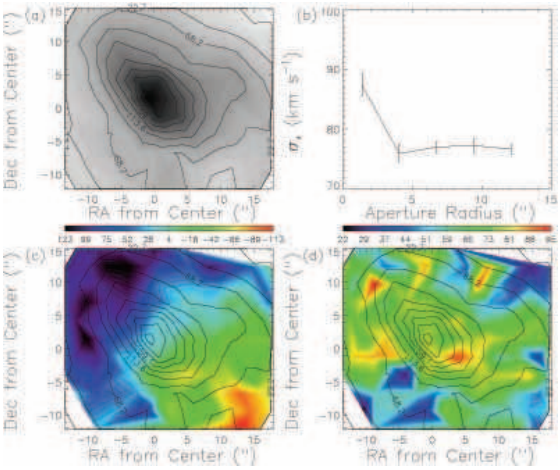

FIG. 21.— Same as Figure 3 but for NGC 4088.

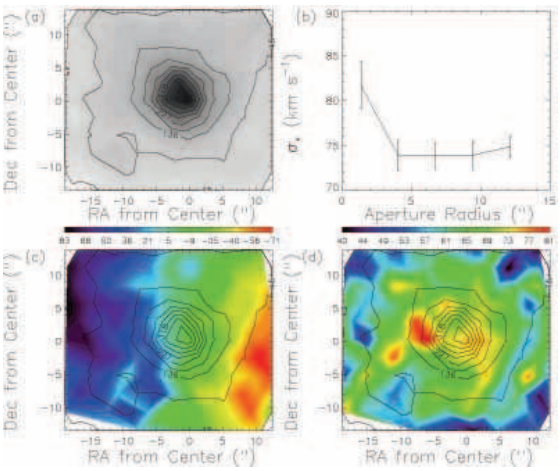

FIG. 22.— Same as Figure 3 but for NGC 4212.

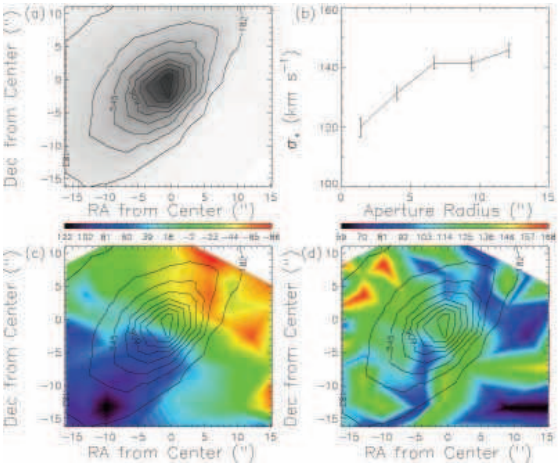

FIG. 23.— Same as Figure 3 but for NGC 4258.

lane (Hughes et al. 2003). The curve of growth shows a steep drop toward the center.

4.19. *NGC 4303*

Figures 24 and 26(d). Good S/N and typical discordance. There is clear offset rotation and a patchy σ_* field. Significant difference between extended and central σ_*.

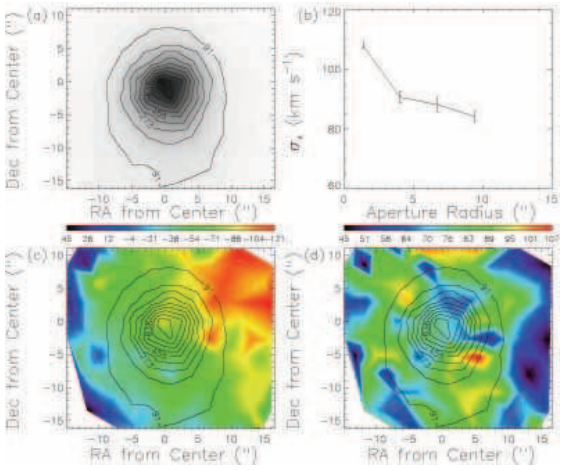

FIG. 24.— Same as Figure 3 but for NGC 4303.

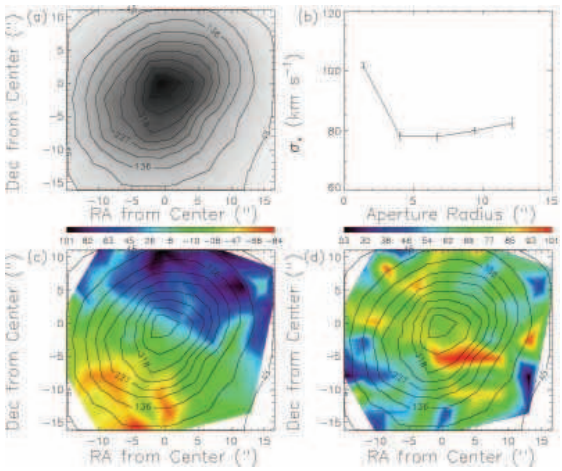

FIG. 25.— Same as Figure 3 but for NGC 4321.

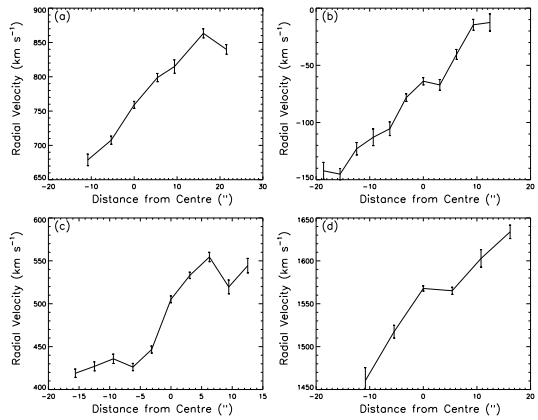

FIG. 26.— Same as Figure 10 but for (a) NGC 4088 [30]. (b) NGC 4212 [90]. (c) NGC 4258 [120]. (d) NGC 4303 [120].

Nuclear spiral structure (Hughes et al. 2003).

4.20. *NGC 4321*

Figures 25 and 30(a). Low discordance and good S/N. Clear peak in σ_* offset from the photometric center. Clear regular rotation and a centrally peaked curve of growth.

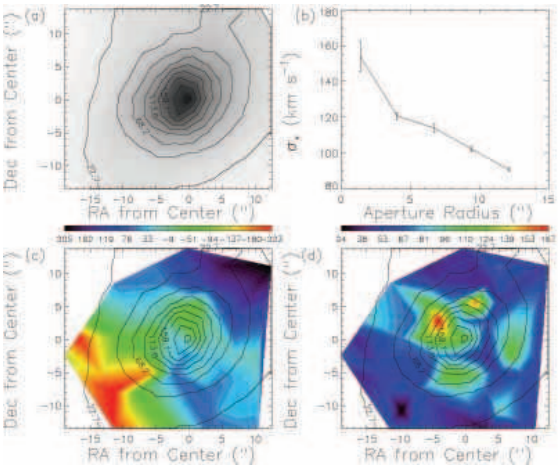

FIG. 27.— Same as Figure 3 but for NGC 4536.

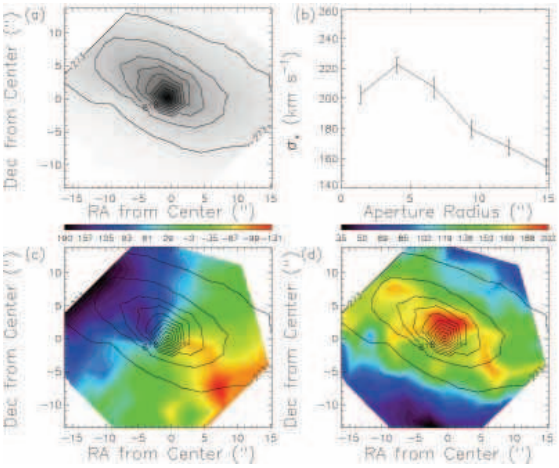

FIG. 28.— Same as Figure 3 but for NGC 5005.

4.21. *NGC 4536*

Figures 27 and 30(b). Significant discordance and very low S/N. Steep rotation and centrally peaked σ_* field. Steep centrally peaked curve of growth. High inclination ($\sim 69°$) and obscuring dust present (Hughes et al. 2003).

4.22. *NGC 5005*

Figures 28 and 30(c). Low discordance and excellent S/N. Clear, well defined rotation and complex σ_* field. Highly variable curve of growth. Large inclination ($\sim 67°$) and complicated dust morphology (Hughes et al. 2003). These are the first measures of σ_* in NGC 5005.

4.23. *NGC 5055*

Figures 29 and 30(d). Low discordance and excellent S/N. Constant curve of growth and clear, well defined rotation. Patchy σ_* field.

5. SUMMARY AND DISCUSSION

In order to populate the low mass regimes of the SMBH - host relations we have completed a STIS survey of 54 bulges in spiral galaxies from which to derive the SMBH mass from gas kinematics (Marconi et al. 2003; Atkinson et al. 2005). To place these points on the relations we need to determine the dynamical properties of the host bulges. To this end we have initiated the

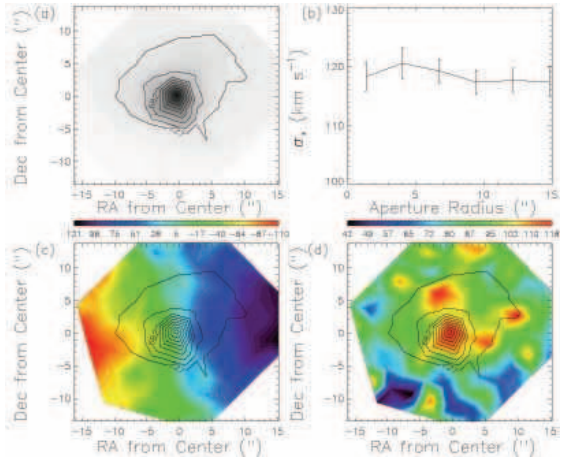

FIG. 29.— Same as Figure 3 but for NGC 5055.

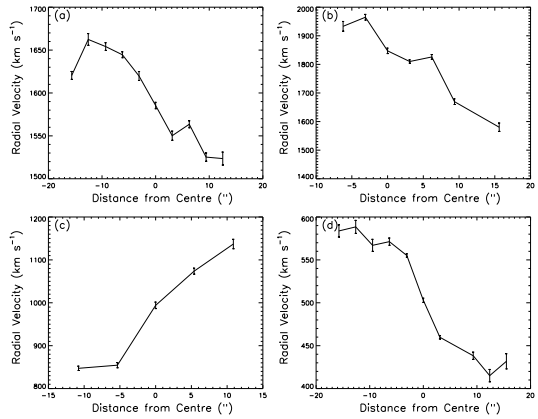

FIG. 30.— Same as Figure 10 but for (a) NGC 4321 [120]. (b) NGC 4536 [120]. (c) NGC 5005 [30]. (d) NGC 5055 [90].

first IFS survey specifically directed toward spiral bulges. We have presented an atlas of 23 spiral bulges, eleven of which do not have previous estimates of σ_*.

The properties of the LOSVDs were derived using the methods of Cross Correlation (Xcor) and Maximum Penalized Likelihood. Each method was thoroughly tested against a simulated system and are robust to spectral contamination from AGN and starbursts.

Where the S/N has allowed we see that each system shows clear coherent radial rotation and patchy irregular velocity dispersion fields. This type of behaviour is displayed in a number of systems observed by SAURON, e.g. NGC 4382 (S0*(s)pec), NGC 4473 (E5) and NGC 4526 (SABO*(s)) (de Zeeuw et al. 2002; Emsellem et al. 2004). We also note that the derived curves of growth, i.e. the variation of σ_* with aperture size, show large variations of σ_* in some cases. Generally we see offsets between the photometric centers of these systems and their peak values of σ_*. We are confident that this observation is also robust in the cases where a large amount of data has been excluded due to low S/N or template mismatching. This discordant data is mainly confined to the outer areas of the Integral Field Spectroscopy arrays where the S/N is at its lowest. As a consequence data at the centers of the arrays are still of high quality (S/N > 14.5). There is also a correlation between the complexity of σ_* fields and the inclination of

the system, especially where it is known that dust obscuration is significant, i.e., in high inclination cases ($\gtrsim 70°$; NGC 2748, NGC 4088, NGC 4258, NGC5005) the larger values of σ_* are confined to a band coincident with the photometric major axis. These observations suggest that σ_* - the projected stellar velocity dispersion - is a non-trivial parameter to derive consistently from system to system.

With these considerations in mind we are left to contemplate the errors in SMBH mass estimates derived from the $M_\bullet - \sigma_*$ relation. The data presented here suggests that values of σ_* taken from the literature, where little heed has been taken of aperture sizes and the effects of rotation, may demonstrate variations due to their heterogeneous nature. An attempt to quantify these errors, with respect to aperture size, can be made by calculating $\delta\bar{\sigma}_*$, i.e. the mean difference between the extended ($\sigma_{\rm ce}$) and central ($\sigma_{\rm cc}$) values of σ_* as determined from Xcor. Indeed, if we are to assume that $\sigma_{\rm ce}$ and $\sigma_{\rm cc}$ are a good representation of σ_* within R_e and $R_e/8$ respectively (R_e being the effective or half-light radius), then $\delta\bar{\sigma}_*$ may also go some way toward explaining the scatter in the $M_\bullet - \sigma_*$ relation, especially in the spiral region where the most weighting is given to the slope (α).

From the data presented in Table 1 we find $\delta\bar{\sigma}_* \approx 20$ km s^{-1}. This figure implies that the slope of the $M_\bullet - \sigma_*$ relation will be affected by the aperture size used to measure σ_*. It then becomes clear that a formal unambiguous definition of σ_* must be made, undoubtedly through the use of Integral Field Spectroscopy where the exact behaviour of σ_* can be followed across two dimensions, before a confident estimate of the slope and scatter in the $M_\bullet - \sigma_*$ relation can be made. It must also be noted that carrying this value of $\delta\bar{\sigma}_*$ through the two forms of the $M_\bullet - \sigma_*$ relation, i.e., $\alpha = 4.72$ (Merritt & Ferrarese 2001) and $\alpha = 4.02$ (Tremaine et al. 2002) using $100 - 120$ km s^{-1}, leads to SMBH mass ranges of $0.49 - 1.17 \times 10^7 M_\odot$ and $0.83 - 1.73 \times 10^7 M_\odot$ respectively. Therefore, in future, authors wishing to use the $M_\bullet - \sigma_*$ relation to estimate the masses of SMBHs from "simple" σ_* measurements must pay close attention to the processes used in order to make that estimate of σ_* in the first place.

Partial support for this work was obtained from a PPARC studentship. We wish to thank the anonymous referee for contributing useful comments and suggestions that have improved the paper. The WHT is operated on the island of La Palma by the Isaac Newton Group in the Spanish Observatorio del Roque de los Muchachos of the Instituto de Astrofisica de Canarias. The AAT is operated by the AAO on behalf of the astronomical communities of Australia and the UK.

Facilities: ING:Herschel(IFU INTEGRAL), AAT(IFU SPIRAL)

REFERENCES

Atkinson, J. el al. 2005, MNRAS in press, astroph/0502573
Alonso-Herrero, A., Ryder, S. D. & Knapen, J. H. 2001, MNRAS, 322, 757
Bender, R. 1990, A&A, 229, 441
Cappellari, M., & Emsellem, E. 2004, PASP, 116, 138
de Zeeuw, P. T., et al. 2002, MNRAS, 329, 513
Dressler, A. 1984, ApJ, 286, 97
Emsellem, E. et al. 2004, MNRAS, 352, 721
Ferrarese, L. & Merritt, D. 2000, ApJ, 539, L9
Franx, M., Illingworth, G. & Heckman, T. 1989, ApJ, 344, 613
Gebhardt et al. 2000, ApJ, 539, L13
Graham, A. W., Erwin, P., Caon, N. & Trujillo, I. 2003, RevMexAA, 17, 196
Hughes, M. A. et al. 2003, AJ, 126, 742
Kormendy, J. & Richstone, D. O. 1995, ARAA, 33, 581
Kuijken, K. & Merrifield, M. R. 1993, MNRAS, 264, 712
Kurtz, M. J & Mink, D. J. 1998, PASP, 110, 934
Laor, A. 2001, ApJ, 553, 677
Magorrian, J. et al. 1998, AJ, 115, 2285
Marconi, A. & Hunt, L. K. 2003, ApJL, 589, L21
Marconi, A. et al. 2003, ApJ, 586, 868
Merritt, D. 1997, AJ, 114, 228
Merritt, D. & Ferrarese. L. 2001, ApJ, 547, 140
Rix, H. & White, S. D. M. 1992, MNRAS, 254, 389
Sargent, W. L. W., Schechter, P. L., Boksenberg, A. & Shortridge, K. 1977, ApJ, 212, 326
Scarlata, C., et al. 2004, AJ, 128, 1124
Simkin, S. M. 1974, A&A, 31, 129
Tonry, J. & Davies, M. 1979, AJ, 84, 1511
Tremaine, S., et al. 2002, ApJ, 574, 740
van der Marel, R. P. & Franx, M. 1993, ApJ, 407, 525